

DYNAMIC OPTICAL COHERENCE ELASTOGRAPHY: A REVIEW

XING LIANG^{*,§}, VASILICA CRECEA^{†,§} and STEPHEN A. BOPPART^{‡,§,¶}

^{*}*Department of Electrical and Computer Engineering*

[†]*Department of Physics*

[‡]*Departments of Electrical and Computer Engineering
Bioengineering, and Internal Medicine*

[§]*Biophotonics Imaging Laboratory
Beckman Institute for Advanced Science and Technology
University of Illinois at Urbana-Champaign
Urbana, IL, 61801, USA*

[¶]*boppart@illinois.edu*

With the development of optical coherence tomography, the application optical coherence elastography (OCE) has gained more and more attention in biomechanics for its unique features including micron-scale resolution, real-time processing, and non-invasive imaging. In this review, one group of OCE techniques, namely dynamic OCE, are introduced and discussed including external dynamic OCE mapping and imaging of *ex vivo* breast tumor, external dynamic OCE measurement of *in vivo* human skin, and internal dynamic OCE including acoustomotive OCE and magnetomotive OCE. These techniques overcame some of the major drawbacks of traditional static OCE, and broadened the OCE application fields. Driven by scientific needs to engineer new quantitative methods that utilize the high micron-scale resolution achievable with optics, results of biomechanical properties were obtained from biological tissues. The results suggest potential diagnostic and therapeutic clinical applications. Results from these studies also help our understanding of the relationship between biomechanical variations and functional tissue changes in biological systems.

Keywords: Optical coherence tomography; optical coherence elastography; biomechanics; tissue characterization; scattering; phase measurements.

1. Introduction

Optical coherence elastography (OCE) is a novel elastography technology used to determine tissue biomechanical properties utilizing the *in vivo* imaging modality optical coherence tomography (OCT). The relationship between OCT and OCE is analogous to ultrasound sonography and elastography. With the inherent advantages of OCT, such as high resolution, non-invasive and real-time imaging, and millimeter-scale penetration depth in tissue, OCE

techniques are unique for measuring or imaging biomechanical properties at the micron-scale tissue level, the cellular level, and even the molecular level.

Since the first demonstration of OCT in 1991,¹ there have been various applications utilizing OCT methods, among which OCE was one to provide contrast based on sample mechanical properties. The first OCE technique was reported in 1998 based on a time-domain OCT (TD-OCT) system.²

The hardware and theory of operation of OCE were described and internal displacements indicating biomechanical properties of gelatin phantoms, pork meat and *in vivo* skin were shown by using a 2D cross-correlation speckle tracking algorithm. Since then, slow external mechanical excitation and static elastography based on speckle tracking methods (or cross-correlation algorithms in OCE) have been established for this technology. The displacement sensitivity for this method was proportional to the axial resolution of the OCT system, which was usually several microns in tissues. The cross-correlation algorithms for OCE were later improved based on the scale of tissue displacements. Two approaches for speckle tracking OCE were studied where one was appropriate for small speckle motions and the other for large, rapid speckle motions.³ An indentation method was combined with static OCE for estimation of material mechanical properties.⁴ Most recently, OCE was combined with polarization sensitive OCT and was used to assess stress distribution in materials in a contact-free and non-destructive manner.⁵

Dynamic OCE was achieved using TD-OCT systems based on a Bessel frequency spectrum of the interferometric OCT signal, and was performed on *in vivo* human skin using a piezoelectric (PZT) ring.^{6,7} A phase-sensitive OCE method was introduced later in 2007⁸ when Fourier-domain OCT (FD-OCT) systems were widely used, from which the phases measurements of the complex OCT data were more stable than in TD-OCT systems. Deformations, strain rates, and strains of soft tissue were measured by this method in real time with a sensitivity on the nanometer scale. This method exploits the phase information available in the complex OCT images and measures the phase changes between successive B-scans to resolve the instantaneous tissue deformations.

OCE techniques have also been widely applied in different fields for biomechanical property measurements. For example, OCT has been investigated for intravascular imaging as a counterpart to intravascular ultrasound imaging, but offering higher spatial resolution. Intravascular OCE was studied to exploit prior information about arterial wall biomechanics to produce robust estimates of tissue velocity and strain.⁹ OCE was also studied as a method for assessing the biomechanical properties of atherosclerotic plaques in which tissue phantoms and aorta were examined *in vitro*

to quantify speckle modulation and measure the displacement and strain maps.¹⁰ An OCE system was used for tissue elasticity reconstruction and distribution results from four representative tissue block models in intravascular imaging.¹¹ Quantitative results such as axial displacement maps were achieved from atherosclerotic arterial samples.¹² Then, a robust algorithm based on correlations between neighboring lines in the OCT image was used for an intravascular OCE study, which offered detection of strains larger than 0.6% in response to an oscillatory force applied to the vessel wall.¹³ A finite element simulation method was combined with OCE to estimate biomechanical properties of vascular tissues.¹⁴ OCE was applied to measure the biomechanical properties of engineered and developing tissues as well. Spatially distributed mechanical displacements and strains were mapped in a representative model of a developing engineered tissue as cells began to proliferate and attach within a 3D collagen matrix. Displacements were quantified by a cross-correlation algorithm on pre- and post-compression images, from which OCE was able to differentiate changes in strain over time, which corresponded with cell proliferation and matrix deposition as confirmed with histological observations. OCE was also performed in the complex developing tissue of the *Xenopus laevis* (African frog) tadpole.¹⁵

OCE has become a very important branch of OCT research and applications. Following the technological developments of OCT, OCE has also been improved both in hardware refinement and algorithm optimization. In addition, OCE provides complementary information for structural OCT images, and thus has the potential to improve sensitivities and specificities in biological and clinical applications of OCT. Compared with elastography techniques based on other biomedical imaging modalities such as ultrasound and MRI, OCE has the intrinsic advantage of high resolution, and thus promptly found application in intravascular imaging as stated above. In addition to intravascular applications, there are more potential applications for OCE techniques such as in oncology. Pathological changes in the tumor micro-structure such as tumor invasion will lead to different biomechanical properties in tissues. Given the micron-scale resolution, OCE is a proper tool for assessing tumor development, especially during early stages. This review focuses on OCE techniques used to investigate the

biomechanics of breast tumor and skin, since these two tissues often involve biomechanical variations during specific pathological changes. Stiff lumps or masses are common during the development of breast cancer, while the most common form of skin cancer, basal cell carcinoma, forms softer tissue than normal. To more effectively detect and minimize the impact and mortality of these diseases, accurate micron-scale detection is key, which will likely involve high-resolution biomechanical property measurements and imaging.

2. Classification of OCE

OCE techniques can be classified in different ways. Based on different spatial excitation characteristics, OCE techniques can be classified as internal excitation or external excitation, while based on different temporal excitation characteristics, OCE techniques can be classified as either static or dynamic, as shown in Fig. 1. Most conventional OCE techniques fall into the static, external excitation OCE group. Thermal elastic optical Doppler tomography can be classified as static, internal excitation OCE, and was reported for measuring phantom mechanical properties.¹⁶ In this review, we focus on dynamic OCE techniques and their applications. In the dynamic, external excitation OCE group, dynamic OCE mapping and imaging techniques and their applications on *ex vivo* breast tumor biomechanical properties are discussed in Sec. 3.1. Dynamic OCE for measurements of biomechanical properties on *in vivo* human skin are discussed in Sec. 3.2. In the dynamic, internal excitation OCE group, acoustomotive OCE (AM-OCE) and magnetomotive OCE (MM-OCE) techniques are discussed in Secs. 4.1 and 4.2, respectively.

Static OCE studies were usually based on speckle tracking methods (or cross-correlation

algorithms in OCE), which have an intrinsic problem. Speckles are granular-shaped patterns in OCT images which result from the convolution of the beam point spread function and the scatterers in the tissue. The speckle pattern is determined by the distances between the scatterers inside the coherence volume.¹⁷ In conventional OCE, a speckle may not have the same signal amplitude or shape before and after deformation of the sample. This problem may cause inaccuracy in traditional static OCE methods. Furthermore, as in all static elastography techniques, static OCE requires knowledge of boundary conditions outside of the region of interest.¹⁸ Dynamic OCE techniques, on the other hand, are able to avoid these drawbacks. However, since they usually rely on solving wave equations, acquisition time or calculation time for these techniques may be problematic for real-time applications.¹⁹

From the spatial excitation characteristics of OCE, external perturbation such as compression and wave propagation are the most common approaches in external excitation OCE techniques. However, as with all external OCE techniques, they often suffer from an inability to maintain a sterile *in vivo* environment. Internal excitation OCE techniques may be able to provide a solution to this problem, but need further investigations for *in vivo* study, which include the delivery of ultrasound pulses or magnetic nanoparticles into living systems.^{20,21}

3. External Dynamic OCE

External excitations are the most common mechanical perturbation methods for OCE techniques. For dynamic OCE techniques, external excitations are usually from mechanical wave sources such as mechanical wave drivers and PZT devices. A variety of types of external excitation have been applied to dynamic OCE techniques, including stretch, compression, and wave propagation. The OCT system used in all the OCE techniques discussed in this review is a lab-based spectral domain OCT (SD-OCT) system, as shown in Fig. 2. In this system, the low-coherence light source consists of a neodymium-doped yttrium orthovanadate (Nd:YVO₄) pumped titanium: sapphire laser, which has a center wavelength of 800 nm and a bandwidth of 100 nm, providing an axial resolution of $\sim 3 \mu\text{m}$ in tissue or tissue phantoms. A 12.5 mm diameter, 40 mm focal length lens was used in the sample arm to provide a transverse resolution of $13 \mu\text{m}$. The average power

	Static	Dynamic
External Excitation	Most traditional OCE	Dynamic OCE on breast tumor and skin
Internal Excitation	Elastic optical Doppler tomography	Acoustomotive and magnetomotive OCE

Fig. 1. Classification and examples of OCE techniques.

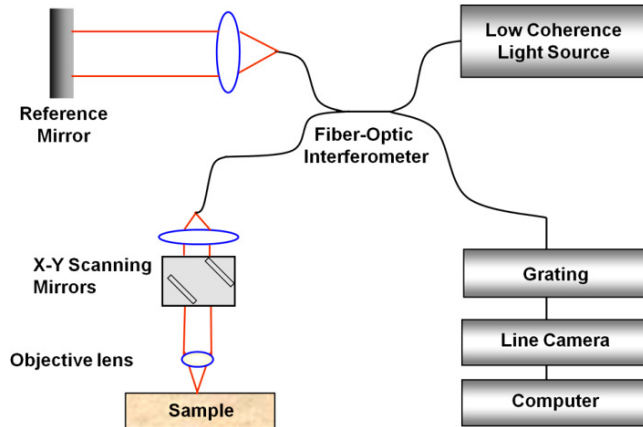


Fig. 2. Schematic diagram of the SD-OCT system used in the dynamic OCE studies.

incident on the samples was 5 to 10 mW. A line charge-coupled device (CCD) camera was used to detect the spectral interference signal with an acquisition rate of 25 kHz. The structural information of the sample is obtained in the spatially-encoded frequency components of the detected OCT signal and then reconstructed by the fast Fourier transform. Since there are no physically moving parts, an SD-OCT system has a much higher stability and acquisition speed than a TD-OCT system.

3.1. External dynamic OCE of *ex vivo* breast tumor

The external dynamic OCE technique was first applied to measure and map biomechanical properties of *ex vivo* human breast tumor.¹⁹ In this OCE system, a glass window stage was fixed in the OCT sample arm to restrict the upper boundary of the samples, yet enable optical imaging through the window. The sample stage was mounted on a mechanical wave driver. The external driving waveform was programmed and synchronized with the image acquisition. Samples were mounted between the upper glass window and the sample stage, with only minimal contact and force prior to data acquisition. M-mode OCT images were acquired through the upper glass window while the driving mechanical perturbations were exerted simultaneously through the sample stage, compressing the sample vertically.

Silicone tissue phantoms with different stiffness were used as samples for system calibration. Step and 20 Hz sinusoidal excitation waveforms were

used in the experiments. From the acquired M-mode OCT images, the motion of a single scattering particle was recorded. Based on the Kelvin–Voigt model, mechanical parameters including spring constants and damping parameters were determined by least-square fitting the recorded particle tracks. Elastic moduli calculated from these parameters denoted the elasticity of the sample, which were calibrated by a commercial indentation measurement method.

Using a calibrated OCE system, *ex vivo* human breast tumor tissues diagnosed as invasive ductal carcinoma were used as specimens for the experiments. Using the same methodology and fitting process, the elastic moduli of breast adipose tissue and tumor tissue were determined as 10.68 ± 0.86 kPa and 0.42 ± 0.17 kPa, respectively. However, in OCT amplitude-based images it was difficult to extract and track the motion of a single scatterer in optically dense tissue, such as the neoplastic human breast tissue. Thus, the phase-resolved OCE algorithm was used to measure the displacements of each pixel in OCT phase-based images. The theoretical principle of the phase-resolved OCE method is similar to Doppler OCT.²² Compared with the amplitude-based OCE method, phase-resolved OCE is more sensitive to small displacements of scatterers in the tissue, providing sub-nanometer displacement sensitivity.³ Therefore, it is possible to measure heterogeneous tissue with both tumor and adipose regions and spatially map different biomechanical regions in human tissue on the micro-scale.

In these experiments, sinusoidal M-mode OCE phase data were recorded for every transverse position of the tissue, which can then be represented as a B-mode OCE image. Each set of M-mode phase data represents the motion track of the scatterers within the beam column. By scanning the laser beam transversely across the sample in steps of $15 \mu\text{m}$, OCE data was obtained for every pixel within a two-dimensional tissue cross-section, with acquisition time of about 5 s for each frame. Subsequently, calculations were performed for each pixel to generate a 2D spatial map of the elastic moduli. Using the phase-resolved OCE method, an elasticity map of tissue containing both tumor and normal adipose was derived, as shown in Fig. 3. The B-mode OCT image of the breast tissue is shown in Fig. 3(a), along with the corresponding histology image shown in Fig. 3(b). The measured elasticity map is shown in Fig. 3(c) along with the elasticity error map shown in Fig. 3(d). In Figs. 3(c) and 3(d), white areas denote pixels with OCE signals smaller

than an amplitude threshold, and median filtering was performed on both images.

The external dynamic OCE method has shown the ability to differentiate small biomechanical variations on the micron-scale. This method might offer the potential for early-stage tumor detection, where it was often difficult to differentiate tissue types by the optical scattering properties alone, and certainly when these changes are too small to be detected by more traditional ultrasound or MRI elastography techniques, or by palpation. High sensitivity is another feature of this method, as the calculated error from the experimental results was as low as 0.08%. However, there are some remaining questions about this method. First, the mechanical model does not account for the couplings between tissue regions with different elastic moduli, and thus, the values on the elasticity map represent relative values of the elastic moduli of the

included a curve-fitting algorithm, the computational time may not be proper for real-time applications. Approximately, the computation time is 7 s for each pixel and 10 hours for the 2D spatial map in Fig. 3 using Matlab on a PC with a dual core 2.0 GHz AMD Athlon™ CPU and 2 Gigabytes of memory.

To improve the accuracy and slow processing speed, an improved external and dynamic OCE method was developed to image biomechanical properties of *ex vivo* breast tumor tissues. In this method, instead of acquiring a series of M-mode OCT images, B-mode images were acquired during sinusoidal mechanical compression excitation, and local strain rates were calculated to represent local biomechanical properties. Different excitation frequencies were used to highlight sample regions with distinct mechanical properties. This technique features fast image acquisition and processing

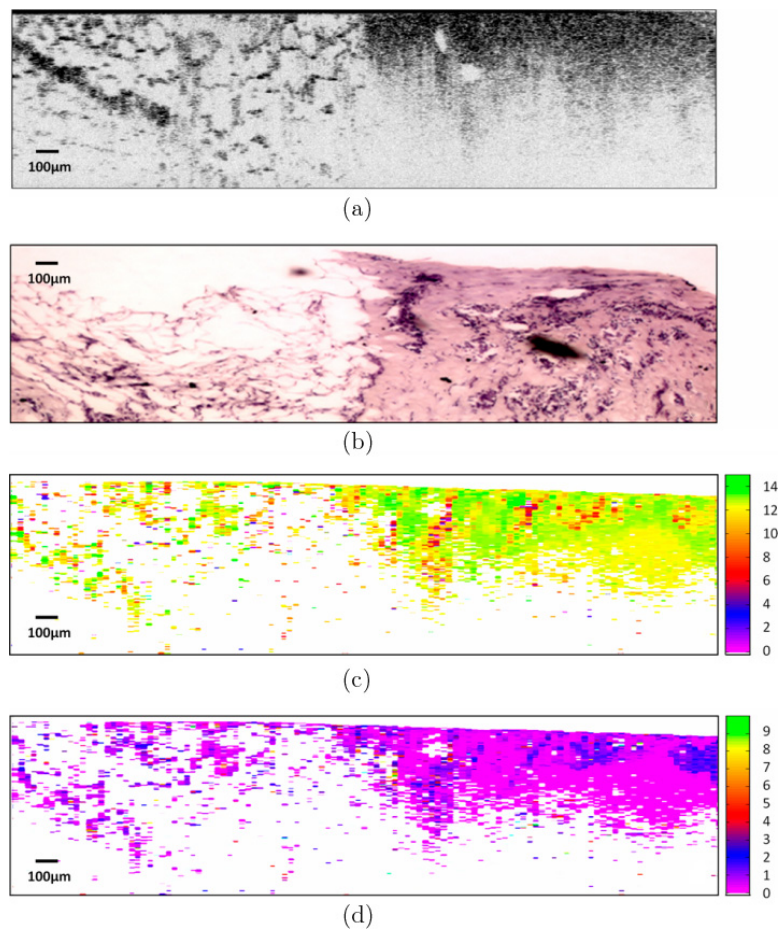


Fig. 3. Phase-resolved OCE map of human breast tissue elasticity. (a) B-mode OCT image of breast tissue. The left side of this image represents adipose tissue while the right side of the image represents tumor tissue. (b) Histology image corresponding to (a). (c) Map of elasticity by sinusoidally driven phase-resolved OCE. (d) Error map of elasticity by sinusoidally driven phase-resolved OCE. Unit for color bar is kPa. Reprinted from Ref. 19 with permission.

speeds, and therefore has the potential for non-destructive volumetric imaging and real-time clinical applications.

The OCE system remained similar to the previous setup, but with the differences that in the OCE sample arm, a fixed 2° round wedge prism was used to restrict the upper boundary of the sample, and a PZT stack was used to bound the bottom of the sample. The PZT stack was used to sinusoidally displace the sample under frequencies of 20 Hz, 45 Hz, 100 Hz, and 313 Hz in the axial direction. Minimal contact and force were applied to the samples prior to data acquisition and a $30 V_{pp}$ sinusoidal voltage signal was applied to the PZT stack during data acquisition, providing $4.5 \mu\text{m}$ maximum displacement.

In this method, OCE images were computed from B-mode OCT spectral datasets that were acquired during dynamic mechanical excitation and acquired with no mechanical excitation. In the transverse direction of the images, a number of cycles of sinusoidal oscillations from the samples were recorded according to the excitation frequency. These oscillations inside the samples were caused by the external excitation, and their amplitudes were determined by both the excitation amplitude and the local mechanical properties of the samples. To extract the mechanical properties of the samples, a reference background OCT image was first subtracted from the datasets, and fast Fourier transformations were taken for each column of the datasets to calculate the complex OCT signals from

the spectral data. The phase was then calculated for each corresponding pixel of the signal, and the phase difference between adjacent A-lines was computed, which was proportional to the scatterer velocities in the axial direction. The phase unwrapping along the transverse dimension was then performed and fast Fourier transformations were taken in the transverse direction to obtain the lateral phase evolution as the motion spectrum. A band-pass filter at the driving frequency and with an appropriate bandwidth was used to select the sample motion under each driving frequency. Thus, after inverse fast Fourier transformation, the sample motion velocities under the driving frequencies were extracted in the OCE phase signal for each pixel. Finally, strain rate calculations and down-sampling were applied to generate the OCE images. To improve specificity, the strain rate images were divided by the ones without any mechanical excitation, and shown in decibels. From the OCE data processing, amplitudes of vibration strain rates of the samples under driving frequencies in the sample were extracted for the OCE images.

A breast tumor rat model was used for this study, and the OCE results from *ex vivo* rat breast tumor tissue are shown in Fig. 4. Figures 4(a) and 4(c) are the OCE images of the tissue under 45 Hz and 313 Hz excitations, respectively. The corresponding OCT structural image and histological image are shown in Figs. 4(b) and 4(d), respectively. From this figure, one can observe that under 45 Hz excitation, the OCE image highlights

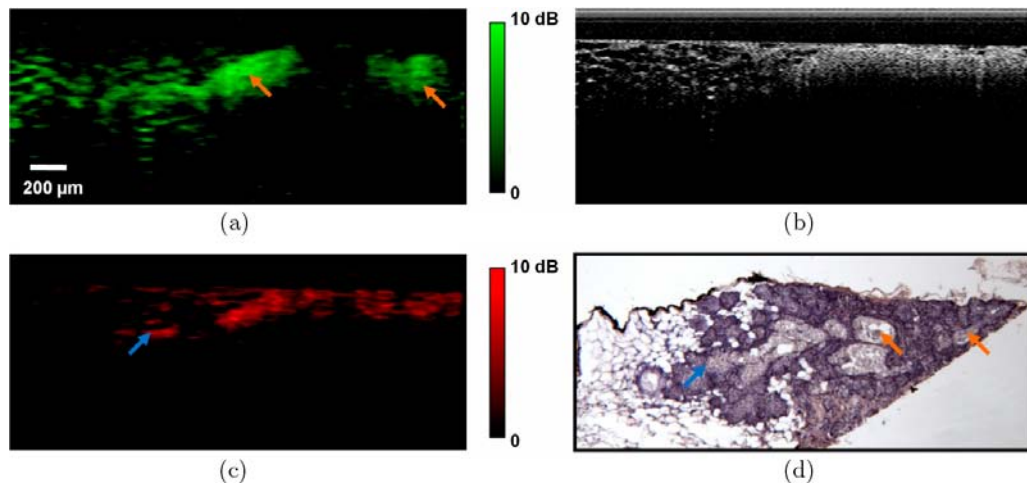


Fig. 4. OCE results of *ex vivo* rat tumor tissue. (a) OCE image under 45 Hz mechanical excitation. (b) OCT structural image of the tissue. (c) OCE image under 313 Hz mechanical excitation. (d) Corresponding histological image. Scale bar applies to all the images. Orange arrows denote adipose cells and connective tissues within tumor, and blue arrows denote invading tumor tissues in fat. Reprinted from Ref. 40 with permission.

predominantly the adipose tissue region (left side of image), while under 313 Hz, the OCE image highlights predominantly the tumor tissue region (right side of image). The 45 Hz and 313 Hz frequencies are near the previously measured mechanical resonances for rat adipose and tumor tissue,²³ respectively. Therefore in the heterogeneous rat tumor tissue, different tissue types were selectively highlighted under different driving frequencies according to their different resonances. Furthermore, in Fig. 4(a), the OCE image includes two regions from the right side (orange arrows) which corresponds to the highly scattering region from the OCT signal. From the histological image, it is shown that this region corresponds to local areas of adipose cells and connective tissues (orange arrows) within the tumor, which is poorly differentiated from the OCT scattering image. On the other hand, the OCE image includes some regions from the left side (blue arrow) which corresponds to the low scattering region from the OCT signal. According to the histological image, those regions correspond to invading tumor tissues in the adipose side (blue arrow).

The image acquisition and processing speeds of this OCE technique have been dramatically improved. The acquisition speed is 4 s per frame for a 1 kHz axial scan rate and 0.8 s per frame for a 10 kHz axial scan rate. The processing speed is approximately 1 s per frame on the same computer using Matlab. With these higher acquisition and processing rates, this dynamic OCE technique has the potential for volumetric biomechanical imaging, and with state-of-the-art OCT hand-held probes, there is also the potential for nondestructive *in vivo* clinical applications using a mechanical actuator design.

3.2. External dynamic OCE of *in vivo* skin

Skin is the other main tissue type of interest for biomechanical property measurements using external dynamic OCE. Much of the research on human skin has mainly focused on reconstruction, transplantation, manipulation, and its use as a tool to assess pharmacologic functions of a variety of toxins, prescription drugs, and cosmetic treatments.²⁴ Skin also maintains many complex physiological functions essential to our survival: fluid homeostasis, immune surveillance, sensory detection, wound healing, and thermoregulation.

Biomechanical properties of skin are of great importance as they contribute to or are responsible for skin health and disease, structural integrity, cosmesis, and aging. In this section, we focus on an external and dynamic OCE method using surface wave propagation and its *in vivo* application for skin structures and biomechanical property measurements.

The SD-OCT system was used for detection of surface wave propagation on skin, and the mechanical wave driver was used for external mechanical excitation, which was synchronized with the OCT system. Sinusoidal waves were generated on the skin surface. The initial distance between the OCT sample arm beam and the mechanical wave driver was chosen arbitrarily to be 16 mm. An M-mode OCT image was recorded at the first position and then the sample arm beam was moved away from the mechanical wave driver at a step distance of 2 mm before the next image was taken. Several step imaging positions were obtained for averaging data for each measurement. Phase data from OCT images were used for the skin displacement detection. Surface wave velocity was first calculated from the OCT phase images, and Young's modulus can be determined.²⁵ By this method, one can quantitatively measure Young's moduli of *in vivo* human skin by OCE.

All *in vivo* experiments were done on the skin of a healthy male volunteer under room temperature and humidity using protocols reviewed and approved by the Institutional Review Board of the University of Illinois at Urbana-Champaign. The skin sites were chosen as relatively flat regions on the volar forearm, dorsal forearm, and palm. A hydrated skin condition was produced by soaking normal skin in a water bath for 20 minutes, followed by a topical application of glycerin for 10 minutes. A dehydrated skin condition was produced by passing heated air from a commercial hair dryer over normal skin for 30 minutes. The OCE results on *in vivo* skin were validated by a commercially available Cutometer (CutometerMPA580, Courage Khazaka Electronic, Koln, Germany), and are shown in Fig. 5.

From the results, one can observe that the frequency-dependent results from dynamic OCE measurements on human skin and skin phantoms are significant. From the literature, it was found that Young's moduli measured with different frequencies correspond to the skin stiffness from different depths.²⁶ At a low surface wave driving frequency, dynamic skin mechanical properties were

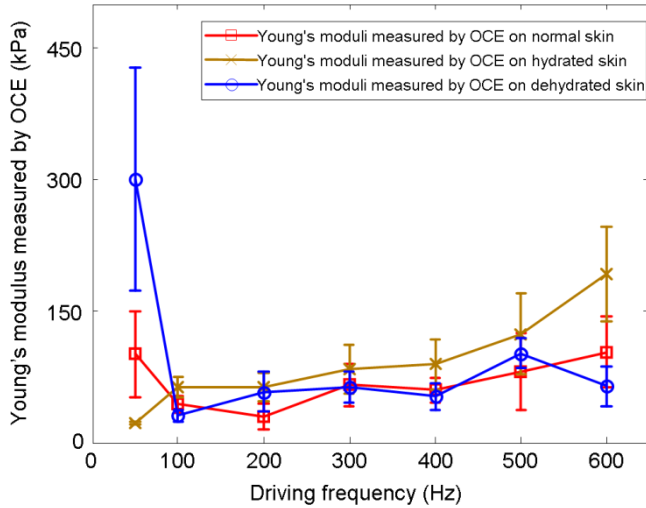


Fig. 5. Young's moduli measured by OCE under different driving frequencies and skin hydration conditions. Blue line denotes results from dehydrated skin, brown line denotes results on hydrated skin, and red line denotes results on normal untreated skin. Reprinted from Ref. 41 with permission.

believed to be primarily due to the outer layer (stratum corneum), while at higher frequencies, the properties were believed to be dominated by the deeper layer (dermis). Based on this theory, the results can be understood as follows. For normal skin, the measured Young's modulus is 101.20 kPa under a 50 Hz driving frequency, which represents the mechanical properties of the stratum corneum. The measured Young's modulus decreases until a driving frequency of 200 Hz and increases again, implying that the epidermis layer has a lower stiffness than the dermis layer. For the hydrated skin, the measured Young's modulus is only 23.01 kPa under a 50 Hz driving frequency, which indicates that the stratum corneum has been softened by the hydrating process. However, the hydrating process tends to increase the stiffness of the skin in the epidermis and dermis layers since the measured Young's moduli are increasing when the driving frequency increases. For the dehydrated skin, the measured Young's modulus is 300.41 kPa under a 50 Hz driving frequency, but for higher frequencies, the measured Young's moduli remain similar to those of normal skin. These findings support and validate the well-known physiology that the outer stratum corneum serves to protect the deeper skin layers against dehydrating conditions.

External dynamic OCE was used to quantitatively measure the Young's modulus of human skin *in vivo*. Compared with other previously used imaging technologies for human skin measurements such

as ultrasound imaging, OCE can differentiate thicknesses with a resolution of several microns, which is critical for resolving different skin layers and their properties. With state-of-the-art OCT hand-held probes, this dynamic OCE technique has the potential in applications of clinical dermatology, plastic surgery, and cosmetic skin assessment.

4. Internal Dynamic OCE

We introduced the studies of external dynamic OCE, and the applications on *ex vivo* breast tumor tissue and *in vivo* human skin. However, according to the implementation characteristics of external excitation methods, it may be difficult to maintain sterile conditions during measurements, which is important when measuring biomechanical properties inside the human body or on exposed tissue surfaces in surgery. In contrast to this, internal and dynamic OCE methods may provide more practical solutions for clinical applications.

4.1. Acoustomotive OCE

The first internal dynamic OCE method is acoustomotive OCE. Acoustic radiation forces have been successfully applied for displacing small lesions that are stiffer than normal tissue to enhance contrast in elastography for abdominal and breast cancers.^{27,28} The AM-OCE technique utilized acoustic radiation forces directly exerted on regions of interest to provide mechanical perturbations, and used SD-OCT to record the displacements to study local biomechanical properties such as in the cancer microenvironment.

The same OCT system as described in Sec. 3.1 was used and the acoustic radiation force was applied by a circular, 19-mm-diameter, f/1 lead PZT element transmitting sine-wave bursts at the resonant frequency of 1 MHz. The PZT element was synchronized with the OCT system as step functions of radiation force were excited into the samples. Gelatin-based phantoms were constructed for AM-OCE measurements due to the need for larger sizes of samples. A stainless steel sphere 1.5 mm in diameter was introduced just prior to gelling to mimic a stiff tissue lesion such as a small tumor. Samples were made for 3% and 4% w/w gel concentrations. The stainless steel sphere was positioned on the beam axis at the 24.5-mm radius of curvature of the ultrasound source. M-mode OCT images of the sphere was recorded. The recorded

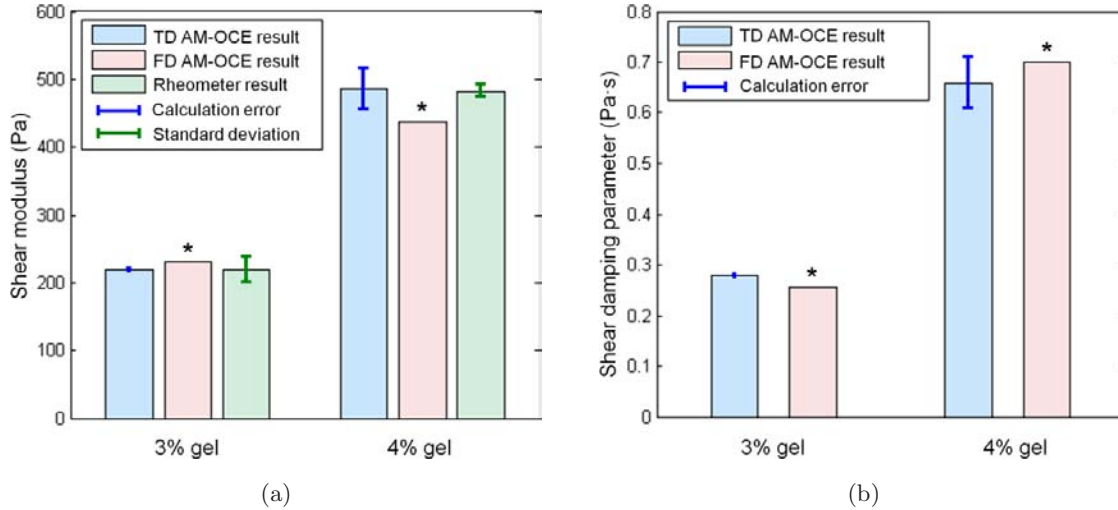


Fig. 6. AM-OCE results on gelatin phantoms. (a) AM-OCE shear modulus. (b) AM-OCE shear damping parameter. The asterisk (*) denotes no statistical or calculation error estimations. Reprinted from Ref. 20 with permission.

OCE data was first analyzed in the time domain, as described in Sec. 3.1. Using the Kelvin–Voigt model and least-square fitting, mechanical parameters including shear modulus and shear damping parameter can be calculated. Following this, the OCE data was also analyzed in the frequency domain. In this method, a fast Fourier transform was used to calculate the spectrum of the recorded data, and by measuring the peak frequency and the -3 dB bandwidth, the material mechanical properties were determined. Finally, the results of measured shear moduli were validated by a rheometer.

These AM-OCE results are shown in Fig. 6. The error bars for the time-domain AM-OCE results represent the calculation errors while the error bars for the rheometer results represent the standard deviations. It can be seen that the AM-OCE results for both samples correspond well with the well-established rheometer results. From the results, one can see that both the shear modulus and shear damping parameters of the gelatin samples double when their concentration increases from 3% to 4%.

No error was estimated for the AM-OCE spectral analysis results because the power spectrum was derived from a single AM-OCE data measurement with no statistical processing or fitting process performed. However, the frequency-domain AM-OCE processing is about five times faster than the time-domain AM-OCE processing. Using the *in vivo* imaging modality OCT for detection, this internal dynamic elastography technique

has great potential for imaging biomechanical properties *in vivo*, especially in quantitatively measuring biomechanical properties of microenvironments around tumor development with micron-scale resolution. For OCE studies on samples without any inclusions, this acoustomotive method is still applicable by using tightly focused acoustic waves.²⁹ Furthermore, the AM-OCE excitation force can be exerted from acoustic radiation originating from outside the body, which makes AM-OCE compatible with a wide range of OCT beam delivery techniques including endoscopes, catheters, and needle-based systems for biomechanical property measurements.

4.2. Magnetomotive OCE

Magnetomotive OCE is another internal dynamic OCE method for internal dynamic OCE for probing the micromechanical properties and microenvironments of viscoelastic materials. After introducing magnetic nanoparticles (MNPs) in the samples, one gains access to the nano- to micro-level interactions between the MNPs and the surrounding microenvironmental matrix by applying a controlled external magnetic field.^{30,31} MM-OCE is conceptually different from previously introduced magnetomotive OCT (MM-OCT),^{30,32–34} because it quantitatively measures the time-dependent oscillations of MNPs and their surrounding microenvironment, and uses this information to determine the viscoelastic properties of the medium. The idea of introducing MNPs for mechanical property measurements had also

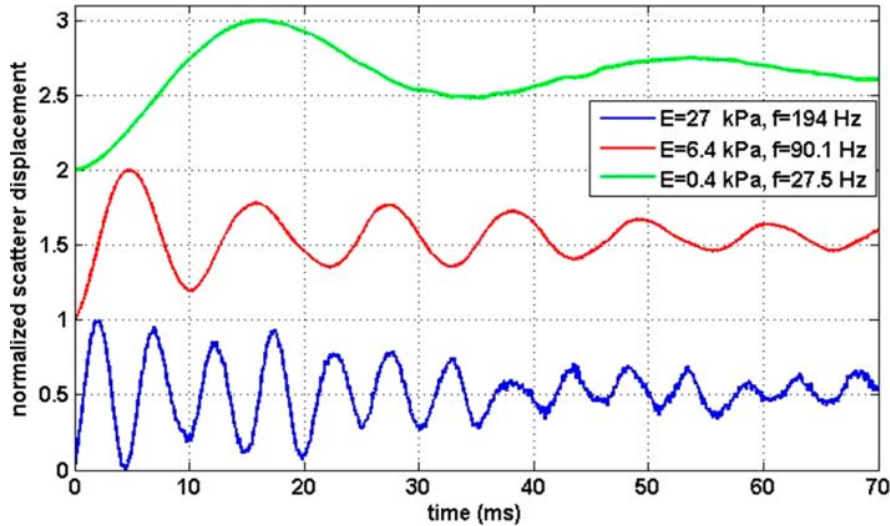


Fig. 7. Normalized measured displacements from samples of different elastic moduli following a step waveform of the applied magnetic field.

been explored for material mechanical spectroscopic studies.³⁵

Silicone tissue phantoms were used as samples for MM-OCE experiments. Resonant frequencies of oscillation of each sample were obtained from the time-resolved displacement of scatterers inside the samples. The curve fitting process as introduced in Sec. 3.1 was used to determine the dominant resonant frequencies of oscillation of the samples. Figure 7 illustrates the normalized scatterer tracks when the field was applied on three samples with different elastic moduli, as validated by indentation measurements. It is observed that the resonant frequency of oscillation varies with the elastic modulus and stiffer samples exhibit higher frequencies. We also tested tissue phantoms with elastic moduli varying between 0.4 and 140 kPa. The results showed that the resonant frequencies closely follow a linear dependence on the square root of the elastic moduli over this range. This range of elastic moduli was representative of the majority of soft polymer composites and matrices as well as biological tissues such as breast tumor, fat, and human skin.

Compared with the other internal OCE methods, MM-OCE has some advantages to mechanically excite tissues. First, this method has the potential to be applied *in vivo*, such as on live animal models with surgically implanted optical windows or exposed tissues. Second, MNPs can be functionalized to target different receptors. For example, antibody-conjugated MNPs have been

demonstrated for targeting molecules from mammary tumors in an animal model.^{36,37} Third, in addition to being a measurement tool, this MM-OCE method also has the potential to function as a therapeutic treatment from induced hyperthermia by magnetic fields.³⁸ Finally, MNPs can be labeled with fluorescent molecules or combined with quantum dots to provide information from microscopic fluorescent imaging techniques as a validation of MM-OCE signals.³⁹

With the ability of MM-OCE to measure a relatively large range of elasticity, our current effort is to quantitatively measure local biomechanical properties of heterogeneous biological tissue such as breast tumor, and map the properties according to B-mode MM-OCT images, such as represented by the images of the rat lung, liver, and muscle, shown in Fig. 8. These MM-OCT images were acquired from *ex vivo* rat tissues, which were immersed in a saline solution with ~ 5 mg/g COOH-MNPs for 40 minutes at room temperature, and rinsed vigorously in pure saline for less than 1 min, and then imaged. The mapping and modeling methods used are similar to the OCE mapping techniques discussed in Sec. 3.1. This approach has the potential to lead to a comprehensive OCT imaging technique, combining multiple contrast mechanisms including structural contrast from OCT, functional molecular contrast from MM-OCT, and mechanical contrast from MM-OCE. This technique also has the potential to enable more accurate diagnostic and therapeutic functions with future OCT developments.

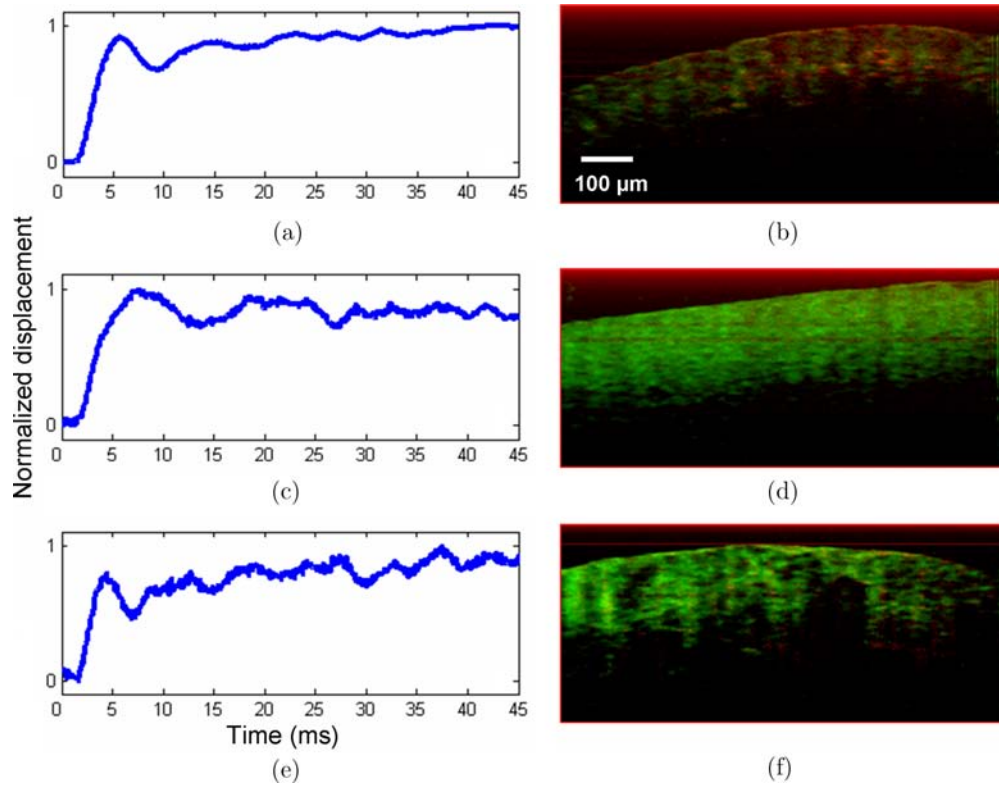


Fig. 8. Normalized MM-OCE measured tissue displacements (step responses) from the application of a switched (off-to-on) magnetic field in biological samples of (a) lung tissue, (c) liver tissue, and (e) muscle tissue from a rat model, and their corresponding MM-OCT images (b, d, and f, respectively). Scale bar applies to all MM-OCT images.

5. Summary and Future Directions

OCT has proved its importance as a biomedical imaging modality, and OCE, which uses varying biomechanical properties as a source for image contrast, is a significant branch of OCT technology. We have focused on dynamic OCE techniques, trying to address some of the intrinsic problems from static or traditional OCE techniques, and at the same time, trying to broaden the applications of OCE and answer more scientific and clinical questions.

In this review, a series of dynamic OCE techniques were presented, including external dynamic OCE mapping and imaging of *ex vivo* breast tumor,^{19,40} external dynamic OCE measurement of *in vivo* human skin,⁴¹ and internal dynamic OCE including acoustomotive OCE²⁰ and magnetomotive OCE.²¹ For each technique, experimental setups, data processing algorithms, and results on measuring or imaging tissue biomechanical properties were presented. Each dynamic OCE technique has different strengths and limitations, along with unique diagnostic capabilities for various applications. However, these dynamic OCE techniques are not limited to the tissues and applications intro-

duced in this review. The concepts and ideas for these dynamic OCE techniques can be easily transferred to optimize existing OCE applications, to improve applications from other elastography techniques, and to explore more fundamental scientific and medical questions. Given the hardware and algorithm features of the dynamic OCE techniques discussed in this review, future efforts may include volumetric OCE on tissues, OCE with hand-held probes, OCE for mechanical spectroscopy, as well as many others. Finally, these techniques also offer the potential for investigating biomechanical properties on the cellular or even molecular scale.

Acknowledgments

We thank Prof. Michael Insana, Prof. Amy Oldenburg, Dr. Steven Adie, Dr. Renu John, Marko Orescanin, and Eric Chaney for their scientific and technical contributions to this work. This work was performed at the Beckman Institute for Advanced Science and Technology at the University of Illinois at Urbana-Champaign, and supported in part by grants from the National Institutes of Health (NIBIB, R21 EB005321, R01

EB005221, R01 EB009073; NCI RC1 CA147096, S.A.B.). Additional information can be found at <http://biophotonics.illinois.edu>.

References

1. D. Huang, E. A. Swanson, C. P. Lin, J. S. Schuman, W. G. Stinson, W. Chang, M. R. Hee, T. Flotte, K. Gregory, C. A. Puliafito, J. G. Fujimoto, "Optical coherence tomography," *Science* **254**, 1178–1181 (1991).
2. J. M. Schmitt, "OCT elastography: Imaging microscopic deformation and strain of tissue," *Opt. Express* **3**, 199–211 (1998).
3. S. J. Kirkpatrick, R. K. Wang, D. D. Duncan, "OCT-based elastography for large and small deformations," *Opt. Express* **14**, 11,585–11,597 (2006).
4. Y. Yang, P. O. Bagnaninchi, M. Ahearne, R. K. Wang, K. K. Liu, "A novel optical coherence tomography-based micro-indentation technique for mechanical characterization of hydrogels," *J. R. Soc. Interface* **4**, 1169–1173 (2007).
5. B. Heise, K. Wiesauer, E. Gotzinger, M. Pircher, C. K. Hitztenberger, R. Engelke, G. Ahrens, G. Grutzner, D. Stifter, "Spatially resolved stress measurements in materials with polarisation-sensitive optical coherence tomography: Image acquisition and processing aspects," *Strain* **46**, 61–68 (2010).
6. S. G. Adie, B. F. Kennedy, J. J. Armstrong, S. A. Alexandrov, D. D. Sampson, "Audio frequency *in vivo* optical coherence elastography," *Phys. Med. Biol.* **54**, 3129–3139 (2009).
7. B. F. Kennedy, T. R. Hillman, R. A. McLaughlin, B. C. Quirk, D. D. Sampson, "*In vivo* dynamic optical coherence elastography using a ring actuator," *Opt. Express* **17**, 21,762–21,772 (2009).
8. R. K. Wang, S. Kirkpatrick, M. Hinds, "Phase-sensitive optical coherence elastography for mapping tissue microstrains in real time," *Appl. Phys. Lett.* **90**, 164105 (2007).
9. R. C. Chan, A. H. Chau, W. C. Karl, S. Nadkarni, A. S. Khalil, N. Iftimia, M. Shishkov, G. J. Tearney, M. R. Kaazempur-Mofrad, B. E. Bouma, "OCT-based arterial elastography: Robust estimation exploiting tissue biomechanics," *Opt. Express* **12**, 4558–4572 (2004).
10. J. Rogowska, N. A. Patel, J. G. Fujimoto, M. E. Brezinski, "Optical coherence tomographic elastography technique for measuring deformation and strain of atherosclerotic tissues," *Heart* **90**, 556–562 (2004).
11. A. S. Khalil, R. C. Chan, A. H. Chau, B. E. Bouma, M. R. Kaazempur-Mofrad, "Tissue elasticity estimation with optical coherence elastography: Toward mechanical characterization of *in vivo* soft tissue," *Ann. Biomed. Eng.* **33**, 1631–1639 (2005).
12. J. Rogowska, N. Patel, S. Plummer, M. E. Brezinski, "Quantitative optical coherence tomographic elastography: Method for assessing arterial mechanical properties," *Br. J. Radiol.* **79**, 707–711 (2006).
13. G. van Soest, F. Mastik, N. de Jong, A. F. van der Steen, "Robust intravascular optical coherence elastography by line correlations," *Phys. Med. Biol.* **52**, 2445–2458 (2007).
14. R. Karimi, T. Zhu, B. E. Bouma, M. R. Kaazempur-Mofrad, "Estimation of nonlinear mechanical properties of vascular tissues via elastography," *Cardiovasc. Eng.* **8**, 191–202 (2008).
15. H. J. Ko, W. Tan, R. Stack, S. A. Boppart, "Optical coherence elastography of engineered and developing tissue," *Tissue Eng.* **12**, 63–73 (2006).
16. Q. Wang, Y.-C. Ahn, C. Kim, L. Yu, W. Jia, B. Rao, Z. Chen, H. K. Chiang, "Thermoelastic optical Doppler tomography of biological tissues," *Proc. SPIE* **6847**, 68471B (2008).
17. J. M. Schmitt, S. H. Xiang, K. M. Yung, "Speckle in optical coherence tomography," *J. Biomed. Opt.* **4**, 95–105 (1999).
18. J. F. Greenleaf, M. Fatemi, M. Insana, "Selected methods for imaging elastic properties of biological tissues," *Annu. Rev. Biomed. Eng.* **5**, 57–78 (2003).
19. X. Liang, A. L. Oldenburg, V. Crecea, E. J. Chaney, S. A. Boppart, "Optical micro-scale mapping of dynamic biomechanical tissue properties," *Opt. Express* **16**, 11,052–11,065 (2008).
20. X. Liang, M. Orescanin, K. S. Toohey, M. F. Insana, S. A. Boppart, "Acoustomotive optical coherence elastography for measuring material mechanical properties," *Opt. Lett.* **34**, 2894–2896 (2009).
21. V. Crecea, A. L. Oldenburg, X. Liang, T. S. Ralston, S. A. Boppart, "Magnetomotive nanoparticle transducers for optical rheology of viscoelastic materials," *Opt. Express* **17**, 23,114–23,122 (2009).
22. L. Wang, Y. M. Wang, S. G. Guo, J. Zhang, M. Bachman, G. P. Li, Z. P. Chen, "Frequency domain phase-resolved optical Doppler and Doppler variance tomography," *Optics Communications* **242**, 345–350 (2004).
23. X. Liang, S. A. Boppart, "Dynamic optical coherence elastography and applications," *Proc. SPIE* **7634**, 763403 (2009).
24. D. A. Medalie, S. A. Eming, M. E. Collins, R. G. Tompkins, M. L. Yarmush, J. R. Morgan, "Differences in dermal analogs influence subsequent pigmentation, epidermal differentiation, basement membrane, and rete ridge formation of transplanted composite skin grafts," *Transplantation* **64**, 454–465 (1997).
25. A. Bayon, F. Gascon, F. J. Nieves, "Estimation of dynamic elastic constants from the amplitude and

- velocity of Rayleigh waves,” *J. Acoust. Soc. Am.* **117**, 3469–3477 (2005).
26. R. O. Potts, D. A. Chrisman, Jr., E. M. Buras, Jr., “The dynamic mechanical properties of human skin *in vivo*,” *J. Biomech.* **16**, 365–372 (1983).
 27. B. J. Fahey, R. C. Nelson, D. P. Bradway, S. J. Hsu, D. M. Dumont, G. E. Trahey, “*In vivo* visualization of abdominal malignancies with acoustic radiation force elastography,” *Phys. Med. Biol.* **53**, 279–293 (2008).
 28. E. J. Chen, R. S. Adler, P. L. Carson, W. K. Jenkins, W. D. O’Brien, Jr., “Ultrasound tissue displacement imaging with application to breast cancer,” *Ultrasound Med. Biol.* **21**, 1153–1162 (1995).
 29. K. R. Nightingale, M. L. Palmeri, R. W. Nightingale, G. E. Trahey, “On the feasibility of remote palpation using acoustic radiation force,” *J. Acoust. Soc. Am.* **110**, 625–634 (2001).
 30. A. L. Oldenburg, J. R. Gunther, S. A. Boppart, “Imaging magnetically labeled cells with magnetomotive optical coherence tomography,” *Opt. Lett.* **30**, 747–749 (2005).
 31. E. P. Furlani, “Magnetophoretic separation of blood cells at the microscale,” *J. Phys. D — Appl. Phys.* **40**, 1313–1319 (2007).
 32. A. L. Oldenburg, F. J. J. Toublan, K. S. Suslick, A. Wei, S. A. Boppart, “Magnetomotive contrast for *in vivo* optical coherence tomography,” *Opt. Express* **13**, 6597–6614 (2005).
 33. A. L. Oldenburg, V. Crecea, S. A. Rinne, S. A. Boppart, “Phase-resolved magnetomotive OCT for imaging nanomolar concentrations of magnetic nanoparticles in tissues,” *Opt. Express* **16**, 11,525–11,539 (2008).
 34. R. John, E. J. Chaney, S. A. Boppart, “Dynamics of magnetic nanoparticle-based contrast agents in tissues tracked using magnetomotive optical coherence tomography,” *IEEE J. Select. Topics Quantum Electronics* **16**, 691–697 (2010).
 35. A. L. Oldenburg, S. A. Boppart, “Resonant acoustic spectroscopy of soft tissues using embedded magnetomotive nanotransducers and optical coherence tomography,” *Phys. Med. Biol.* **55**, 1189–1201 (2010).
 36. J. H. Lee, Y. M. Huh, Y. W. Jun, J. W. Seo, J. T. Jang, H. T. Song, S. Kim, E. J. Cho, H. G. Yoon, J. S. Suh, J. Cheon, “Artificially engineered magnetic nanoparticles for ultra-sensitive molecular imaging,” *Nat. Med.* **13**, 95–99 (2007).
 37. R. John, R. Rezaeipoor, S. G. Adie, E. J. Chaney, A. L. Oldenburg, M. Marjanovic, J. P. Haldar, B. P. Sutton, S. A. Boppart, “*In vivo* magnetomotive optical molecular imaging using targeted magnetic nanoprobe,” *Proc. Natl. Acad. Sci. USA* **107**, 8085–8090 (2010).
 38. S. J. DeNardo, G. L. DeNardo, L. A. Miers, A. Natarajan, A. R. Foreman, C. Gruettner, G. N. Adamson, R. Ivkov, “Development of tumor targeting bioprobes ((111)In-chimeric L6 monoclonal antibody nanoparticles) for alternating magnetic field cancer therapy,” *Clin. Cancer Res.* **11**, 7087s–7092s (2005).
 39. R. Koole, W. J. Mulder, M. M. van Schooneveld, G. J. Strijkers, A. Meijerink, K. Nicolay, “Magnetic quantum dots for multimodal imaging,” *Wiley Interdiscip. Rev. Nanomed. Nanobiotechnol.* **1**, 475–491 (2009).
 40. X. Liang, S. G. Adie, R. John, S. A. Boppart, “Dynamic spectral-domain optical coherence elastography for tissue characterization,” *Opt. Express* **18**, 14,183–14,190 (2010).
 41. X. Liang, S. A. Boppart, “Biomechanical properties of *in vivo* human skin from dynamic optical coherence elastography,” *IEEE Trans. Biomed. Eng.* **57**, 953–959 (2009).